



# The complete patient QA system



3D patient plan QA



3D IMRT/VMAT pre-treatment QA



3D in vivo daily treatment QA



Online patient positioning QA

## Upgrade your patient safety by bridging the gap between patient QA and machine QA

DoseLab<sup>®</sup> machine QA software, the complete TG-142 solution, is now integrated into the Mobius3D<sup>®</sup> patient QA system!

Visit [mobiusmed.com/mobius3d](http://mobiusmed.com/mobius3d) to learn more.

Safety information: Radiation may cause side effects and may not be appropriate for all cancers.

© 2018 Varian Medical Systems, Inc. Varian, Varian Medical Systems, DoseLab and Mobius3D are registered trademarks of Varian Medical Systems, Inc.

varian | MOBIUS

# Towards context-sensitive CT imaging — organ-specific image formation for single (SECT) and dual energy computed tomography (DECT)

Sabrina Dorn<sup>a)</sup>

*German Cancer Research Center (DKFZ), Im Neuenheimer Feld 280, 69120 Heidelberg, Germany*

*Medical Faculty, Ruprecht-Karls-University Heidelberg, Im Neuenheimer Feld 672, 69120 Heidelberg, Germany*

Shuqing Chen

*Pattern Recognition Lab, Friedrich-Alexander-University Erlangen-Nürnberg, Martenstraße 3, 91058 Erlangen, Germany*

Stefan Sawall

*German Cancer Research Center (DKFZ), Im Neuenheimer Feld 280, 69120 Heidelberg, Germany*

*Medical Faculty, Ruprecht-Karls-University Heidelberg, Im Neuenheimer Feld 672, 69120 Heidelberg, Germany*

Joscha Maier

*German Cancer Research Center (DKFZ), Im Neuenheimer Feld 280, 69120 Heidelberg, Germany*

*Department of Physics and Astronomy, Ruprecht-Karls-University, Im Neuenheimer Feld 226, 69120 Heidelberg, Germany*

Michael Knaup, Monika Uhrig, and Heinz-Peter Schlemmer

*German Cancer Research Center (DKFZ), Im Neuenheimer Feld 280, 69120 Heidelberg, Germany*

Andreas Maier

*Pattern Recognition Lab, Friedrich-Alexander-University Erlangen-Nürnberg, Martenstraße 3, 91058 Erlangen, Germany*

Michael Lell

*Department of Radiology and Nuclear Medicine, Klinikum Nürnberg, Paracelsus Medical University, Prof.-Ernst-Nathan-Strasse 1, 90419 Nürnberg, Germany*

Marc Kachelrieß

*German Cancer Research Center (DKFZ), Im Neuenheimer Feld 280, 69120 Heidelberg, Germany*

*Medical Faculty, Ruprecht-Karls-University Heidelberg, Im Neuenheimer Feld 672, 69120 Heidelberg, Germany*

(Received 19 April 2018; revised 30 July 2018; accepted for publication 3 August 2018;

published xx xxxx xxxx)

**Purpose:** The purpose of this study was to establish a novel paradigm to facilitate radiologists' workflow — combining mutually exclusive CT image properties that emerge from different reconstructions, display settings and organ-dependent spectral evaluation methods into a single context-sensitive imaging by exploiting prior anatomical information.

**Methods:** The CT dataset is segmented and classified into different organs, for example, the liver, left and right kidney, spleen, aorta, and left and right lung as well as into the tissue types bone, fat, soft tissue, and vessels using a cascaded three-dimensional fully convolutional neural network (CNN) consisting of two successive 3D U-nets. The binary organ and tissue masks are transformed to tissue-related weighting coefficients that are used to allow individual organ-specific parameter settings in each anatomical region. Exploiting the prior knowledge, we develop a novel paradigm of a context-sensitive (CS) CT imaging consisting of a prior-based spatial resolution (CSR), display (CSD), and dual energy evaluation (CSDE). The CSR locally emphasizes desired image properties. On a per-voxel basis, the reconstruction most suitable for the organ, tissue type, and clinical indication is chosen automatically. Furthermore, an organ-specific windowing and display method is introduced that aims at providing superior image visualization. The CSDE analysis allows to simultaneously evaluate multiple organs and to show organ-specific DE overlays wherever appropriate. The ROIs that are required for a patient-specific calibration of the algorithms are automatically placed into the corresponding anatomical structures. The DE applications are selected and only applied to the specific organs based on the prior knowledge. The approach is evaluated using patient data acquired with a dual source CT system. The final CS images simultaneously link the indication-specific advantages of different parameter settings and result in images combining tissue-related desired image properties.

**Results:** A comparison with conventionally reconstructed images reveals an improved spatial resolution in highly attenuating objects and in air while the compound image maintains a low noise level in soft tissue. Furthermore, the tissue-related weighting coefficients allow for the combination of varying settings into one novel image display. We are, in principle, able to automate and standardize the spectral analysis of the DE data using prior anatomical information. Each tissue type is evaluated with its corresponding DE application simultaneously.

**Conclusion:** This work provides a proof of concept of CS imaging. Since radiologists are not aware of the presented method and the tool is not yet implemented in everyday clinical practice, a comprehensive clinical evaluation in a large cohort might be topic of future research. Nonetheless, the presented method has potential to facilitate workflow in clinical routine and could potentially improve diagnostic accuracy by improving sensitivity for incidental findings. It is a potential step toward the presentation of evermore increasingly complex information in CT and toward improving the radiologists workflow significantly since dealing with multiple CT reconstructions may no longer be necessary. The method can be readily generalized to multienergy data and also to other modalities. © 2018 American Association of Physicists in Medicine [<https://doi.org/10.1002/mp.13127>]

Key words: CT, CNN segmentation, dual energy, image display, image formation

## 1. INTRODUCTION

Computed tomography (CT) is irreplaceable in clinical routine. Multiple disciplines base their therapeutic decisions on CT diagnoses. Indications are manifold and include examinations, for example, in oncological, gastrointestinal, and trauma imaging. However, for one acquired CT rawdata set, there are manifold parameters for CT image reconstruction, display, and analysis. Among others, the reconstruction algorithm and parameters, for example, analytical, iterative, kernel, strength of iterative reconstruction, etc., determine the CT image quality. In particular, the choice of the reconstruction kernel in an analytical reconstruction has a strong impact on competing characteristics of the reconstructed images: soft kernels result in smooth images with high contrast and low noise level but poor spatial resolution. In contrast, sharp kernels provide images not only with high spatial resolution but also high noise levels.<sup>1</sup> Moreover, reading CT images requires organ-dependent display settings. For display purposes, the images are often viewed with varying display settings and blending ratios. The images are reformatted either in axial, coronal, sagittal, oblique, curved, or arbitrary plane. Moreover, different window level settings favor the presentation of different anatomical structures. Especially the lung is recommended to be reconstructed with a lung kernel and viewed in a lung window that is superior compared to a soft tissue gray level window.<sup>2,3</sup> In order to detect lung nodules, this organ is frequently visualized with a (STS) maximum intensity projection (MIP). On the contrary, reading liver images requires a low noise level. The image is therefore displayed using thicker slabs<sup>4,5</sup> although thin slices would be preferable. The image is visualized using a soft tissue gray level window. Furthermore, there are many dual energy (DE) applications, which provide a multitude of information about the tissue type, material composition, or function to the radiologist. However, each of the approved applications processes the entire DECT dataset and performs the DECT evaluation organ- or indication-specific (virtual noncontrast (VNC), iodine overlay, gout visualization, kidney stones, blood flow in the lung or heart, bone marrow, etc.). The dual energy information outside the organ of interest is therefore worthless and cannot be used to improve diagnosis. In the clinical routine, the user needs to invoke each application manually in order to start a specific dual energy evaluation. Supposing

that the user wants to evaluate different body regions, the various applications are called sequentially. Furthermore, each of the applications requires a patient-specific calibration, based on manually placed regions of interest (ROIs). A comprehensive dual energy-based diagnosis involves several user interactions and the interpretation of multiple DE analyses. As a consequence, each medical question requires a case-adapted CT examination and analysis in order to obtain a comprehensive diagnosis for the patient. A large amount of different image stacks need to be interpreted under varying diagnostic questions. Hence, reading CT images and preparing them for interdisciplinary case discussions like tumor boards are a tedious and time-consuming task.

In this paper, we therefore propose an innovative concept of a context-sensitive CT imaging in contrast to the conventional CT imaging with the aim to significantly improve the clinical routine. In this work, we present a novel approach to combine initially mutually exclusive CT image properties that emerge from different reconstructions, display settings and spectral evaluations and analyses into a single context-sensitive imaging by means of prior anatomical information. The novel imaging paradigm now favors the display of only one context-sensitive image volume and enables the interactive adjustment of various organ-specific parameters in real time as well as the smooth changeover back to the conventional imaging during diagnosis. We thus present an end-to-end pipeline that contains a context-sensitive image formation which enforces local image properties. The volumes are displayed organ dependently and can be evaluated and analyzed in an organ-specific manner. In order to provide a proof of concept, we focus on the most common analytic reconstruction kernels, display techniques (windowing and sliding thin slab technique), and dual energy applications in this work. However, the bench of possibilities could be extended as easily. The contributions of this work include the usage of prior anatomical knowledge to allow for an organ-dependent adaptation of different reconstruction algorithms, the use of individually optimized display settings, and the selection of organ-related DE evaluation on a per-voxel basis. Our end-to-end pipeline to permit a context-sensitive (CS) imaging mainly consists of three steps that do not require any user interaction:

1. Perform an automatic multiorgan segmentation (Section 2.A) in varying anatomical regions using a

cascaded three-dimensional (3D) fully convolutional neural network (CNN).

2. Transform the segmentation result to tissue-related weighting coefficients (Section 2.B). The binary-segmented masks are converted to weights that introduce smooth transition zones between the different anatomical regions. The tissue-related weighting coefficient is derived using the squared Euclidean distance transform of the masks.
3. Use the tissue-related coefficients to allow for individual settings for each anatomical region. We present a prior-based organ-specific image formation that consists of a context-sensitive display (CSD) (Section 2.C) and a context-sensitive dual energy evaluation (CSDE) (Section 2.D).

## 2. MATERIALS AND METHODS

### 2.A. Prior anatomical information

In this paper, we assume that an accurate multiorgan segmentation is given. We focus on demonstrating the benefit of incorporating prior anatomical information. Once an assignment between a voxel and an anatomy label is given, the prior knowledge is exploited to provide a more sophisticated anatomy-adapted imaging. In particular, we obtain our segmentations using the method proposed in Ref. [6]. To summarize briefly, the segmentation is obtained by a coarse-to-fine hierarchical 3D fully convolutional neural network (CNN) that is based on the U-net for biomedical image segmentation.<sup>7</sup> A U-net is a fully connected CNN including an analysis and synthesis path. The approach was later extended to 3D volumetric data.<sup>8</sup> A cascaded 3D fully connected CNN segments the single (SECT) or dual energy CT (DECT) data into different organs. In case of SECT data, the image to be segmented is directly passed through the network. In case of DECT data, a mixed image is calculated beforehand. In our used segmentation approach,<sup>6</sup> the mixing weight  $\alpha$  is optimized to maximize the segmentation accuracy. The network architecture is shown in Fig. 1. Each stage is based on a 3D U-net with a depth of four levels.

The first stage of the network is trained and applied to detect the abdominal cavity. This generated ROI reduces the search space and improves the class weights for the multiorgan segmentation. The output of the second stage is a prediction map wherein each value indicates the probability of the voxel belonging to a certain organ. The final segmentation result is consequently defined by the maximum intensity of these class probability maps. The network is implemented using an open source implementation of a two-stage cascaded network<sup>9</sup> and the Caffe deep learning library.<sup>10</sup> The U-net was initialized with pretrained weights.

Our data pool include 42 contrast-enhanced patient DECT scans in the arterial and portal venous phase with varying clinical indications. We used 30 scans for training, 6 for validation, and 6 for testing. The training on 30 cases takes 2–3

days per stage and the final segmentation takes a few minutes. The method achieves an average Dice coefficient over all 42 patients (eightfold cross validation with six test patient datasets, respectively) of  $93 \pm 1\%$  for the liver,  $92 \pm 3\%$  for the spleen,  $91 \pm 3\%$  for the right kidney and  $89 \pm 5\%$  for the left kidney,  $96 \pm 2\%$  for the right lung, and  $96 \pm 1\%$  for the left lung, respectively. To accommodate for different field of views (FOVs), we included scans with varying FOV, ranging from 350 to 500 mm, into our training set. However, the proposed method is sensitive to the scan protocol. A fine-tuning of the parameters might be required if the scan protocol is different and has never been trained.

It is not the main contribution of this work to discuss the details on the automatic segmentation. We apply the proposed approach as it is without any modifications. Using the provided segmentation method, the dataset is segmented into the organs liver, left and right kidney, spleen, aorta, and left and right lungs. The remaining yet unlabeled voxels are further classified into five tissue types bone, muscle, fat, vasculature, and air. We apply a simple thresholding to derive the tissue classes. Since the tissue types are well separable by means of their CT value differences, the thresholds are selected by Otsu's algorithm.<sup>11</sup> If there is a contrast media uptake, the separation between the tissue classes vasculature and bone has to be manually postprocessed, since their CT value distribution is quite similar in only a SECT scan is available for segmentation. In case of DECT data, both materials can be separated based on their material-specific spectral behavior.

### 2.B. Tissue-related weighting coefficients

By means of the automatic segmentation, the target CT dataset is divided into  $L$  disjunct tissue labels, that is, each voxel  $\mathbf{r} = (x, y, z)$  is initially assigned one label  $l$  and the dataset is uniquely characterized. Given these organ or tissue labels, the volume is subdivided into a set of disjunct binary masks  $M = \{m_1(\mathbf{r}), m_2(\mathbf{r}), \dots, m_L(\mathbf{r})\}$  for each label. For our purposes, we intend to use the organ and tissue labels to allow for an organ-dependent parameter adaptation. Since the labels are nonoverlapping, we need smooth tissue-related weighting coefficients  $w_l(\mathbf{r})$  for each label  $l$  from the binary masks. Within the emerging transition zone of adjacent organs, the voxel is no longer exactly assigned to one specific anatomical structure and can be interpreted as an anatomical hybrid voxel. The tissue-related weights can therefore also be interpreted as a prior probability that a voxel belongs to a certain anatomical region. The weight  $w_l(\mathbf{r})$  corresponding to one specific tissue class  $l$  at voxel position  $\mathbf{r}$  is defined as follows

$$w_l(\mathbf{r}) \in \begin{cases} \{1\} & \text{if } \mathbf{r} \text{ belongs to a specific tissue class } l, \\ (0, 1) & \text{if } \mathbf{r} \text{ belongs to the transition area,} \\ \{0\} & \text{elsewhere.} \end{cases} \quad (1)$$

The smooth tissue-related weighting coefficient is derived by a transition zone diameter  $d$  between neighboring regions.

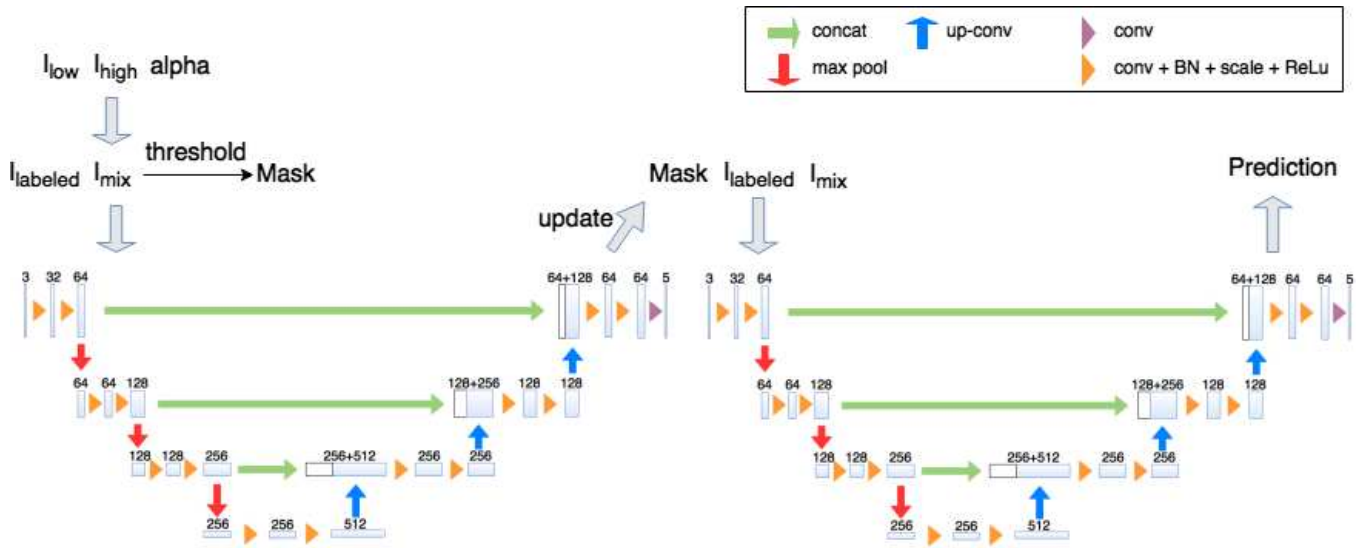


FIG. 1. Architecture of the two cascaded U-nets for DECT multiorgan segmentation.

The width of the transition zone can depend on the initial segmentation and the diameter  $d$  can thus be selected organ dependent. In our case, a constant transition zone diameter is used as we show later on. The tissue-related weight is derived using the Euclidean distance transform<sup>12</sup>  $D$  of each label mask  $m_l(\mathbf{r})$ . The transformation  $D(\mathbf{r}, l)$  associates the distance to the nearest point in the mask  $m_l(\mathbf{r})$  to each voxel  $\mathbf{r}$  in the volume. We then perform a truncation of the Euclidean distance field: if the Euclidean distance is larger than the diameter  $d$ , the transformed values are cropped and set to  $d$ .

$$D_{\text{trunc}}(\mathbf{r}, l) = \begin{cases} d & \text{if } D(\mathbf{r}, l) > d, \\ D(\mathbf{r}, l) & \text{otherwise.} \end{cases} \quad (2)$$

An inverse scaling and normalization to ensure  $\sum_{l=1}^L w_l(\mathbf{r}) = 1$  yields the final tissue-related weight for voxel  $\mathbf{r}$  and label  $l$

$$w_l(\mathbf{r}) = \frac{\frac{1}{d}(d - D_{\text{trunc}}(\mathbf{r}, l))}{\sum_{l=1}^L \frac{1}{d}(d - D_{\text{trunc}}(\mathbf{r}, l))}. \quad (3)$$

Since each voxel  $\mathbf{r}$  is initially assigned to exactly one label, the sum  $\sum_{l=1}^L \frac{1}{d}(d - D_{\text{trunc}}(\mathbf{r}, l))$  is greater than zero for each voxel position.

These weights are used in the following to manage the behavior inside transition zones between adjacent regions in the context-sensitive resolution (CSR), context-sensitive display (CSD), and context-sensitive dual energy evaluation (CSDE).

## 2.C. Context-sensitive display (CSD)

### 2.C.1. Context-sensitive spatial resolution (CSR)

An image is formed that combines mutually exclusive image properties like high spatial resolution inside the bone or lung and low noise level in soft tissue regions. Depending on the assigned label, the basis image most suitable for the

organ, tissue type, and clinical indication is chosen automatically from the set of  $B$  pre-reconstructed basis images  $f_b(\mathbf{r})$  on a per-voxel basis. The basis images can either result from a single or a DECT scan as well as from a monoenergetic reconstruction from dual energy data. It is possible to reconstruct the basis images using varying reconstruction methods, for instance an analytical reconstruction with varying kernels or an iterative reconstruction, resulting in images with desired competing properties.<sup>1,13,14</sup> For reconstruction, we use the weighted filtered backprojection (wFBP)<sup>15</sup> that is available at our scanner (Somatom Definition Flash, Siemens Healthineers, Forchheim, Germany). The basis images are reconstructed with different reconstruction kernels leading to various resolution levels. The CSR is defined as

$$f_{\text{CSR}}(\mathbf{r}) = \sum_{l=1}^L \sum_{b=1}^B w_l(\mathbf{r}) \cdot \delta_{l,b}(\mathbf{r}) \cdot f_b(\mathbf{r}), \quad (4)$$

where  $w_l(\mathbf{r})$  is the tissue-related weighting coefficient,  $\delta_{l,b}$  is the Kronecker delta function that describes the assignment of the label  $l$  to the basis image  $f_b(\mathbf{r})$ .

More than one label might be assigned to the same basis image. For instance, a smooth basis image  $f_{\text{smooth}}(\mathbf{r})$  is assigned to the tissue type classes liver as well as kidney. Thus, more than one anatomical structure may be reconstructed with the same basis image. The basis image  $f_b(\mathbf{r})$  contributes if and only if it is assigned to the label  $l$  meaning that the weight is greater than 0. Inside the artificial overlapping transition zones, a weighted mean of the contributing basis images is calculated. The result is a compound image altering the resolution and noise level depending on the depicted tissue type and organ.

In order to provide an image display that guarantees an optimal image impression, presenting each anatomical structure with the best-adapted display settings simultaneously, we further propose a CSD. The approach is twofold: on the one hand, the CSD locally adapts the window level settings, the

center and the width, for each organ or tissue type separately. The displayed images combine several organ-dependent window level settings. These organ-specific settings are chosen in accordance with recommended settings for individual anatomical regions in the literature<sup>2,3</sup> rather than arbitrarily selected ones to provide an initial parameter selection. However, we are not restricted to these values and an intuitive parameter adaptation is possible at any time during the image presentation. On the other hand, the CSD images can be viewed with an adaptive sliding thin slab (STS) technique. Depending on the desired anatomical structure, the image can be reformatted in an arbitrary direction using, for instance, a piecewise organ-specific STS-mean intensity projection (MeanIP), STS-maximum intensity projection (MIP), and STS-minimum intensity projection (MinIP) simultaneously. An STS-MeanIP is frequently applied in the liver to render the image with almost no noise remaining. An STS-MinIP is often used for the potential diagnosis of an emphysema in the lung.<sup>16</sup> An STS-MIP facilitates, for example, the detection of pulmonary nodules in the lung.<sup>17</sup> The slab thickness are chosen organ dependently. The STS techniques and corresponding slab thicknesses are also selected as recommended in the literature.<sup>4,5</sup> Additional more sophisticated display techniques might be applied in the same manner. The following methods are applicable to the CSR image as well as to every other CT image, for example, single or dual energy data.

### 2.C.2. Adaptive window level settings

The window level settings (center and width) for each tissue type are locally adapted both to the specific organ and to the clinical indication. The above-mentioned tissue-related weighting coefficient is reused to realize a soft blending between neighboring window level settings, for example, lung window vs soft tissue window. We establish an artificial transition area between these adjacent windows by means of a blending weight coefficient for each label  $l$ . Since the blending radius varies from the transition diameter during image composition, this weight is denoted by  $\beta_l(\mathbf{r})$ . The preset or organ-specific diameter determines the overlap between the neighboring regions. The organ-dependent center  $C_{\text{blend}}$  and width  $W_{\text{blend}}$  for each voxel are given by

$$C_{\text{blend}}(\mathbf{r}) = \sum_{l=1}^L \beta_l(\mathbf{r}) \cdot C_l, \quad (5)$$

$$W_{\text{blend}}(\mathbf{r}) = \sum_{l=1}^L \beta_l(\mathbf{r}) \cdot W_l, \quad (6)$$

where  $C_l$  and  $W_l$  are the center and width assigned to the organ or tissue type  $l$ . The organ-specific assignment of the center and the width is not fixed and can be changed dynamically on demand. Within the overlapping areas, a smooth transition between neighboring window/level settings emerges.

### 2.C.3. Adaptive sliding thin slabs (STS)

The CSD can be improved using an adaptive STS display technique. The CT data are no longer displayed as one entire volume but rather as slabs of sections that move through the volume of the dataset.<sup>4</sup> Whenever possible, the CT volumes are reconstructed with the smallest possible slice thickness in order to obtain an isotropic spatial resolution to facilitate a MPR in arbitrary direction. However, an isotropic spatial resolution results in a high noise level that can be reduced by viewing the CT image in thicker “slabs”. Multiple subsequent images are combined, that is, by averaging adjacent parallel slices (STS-mean) along different viewing directions. In our adaptive STS implementation, the slab thicknesses are chosen organ specifically. Furthermore, the mean calculation is substituted by retaining the maximum value (STS-MIP) or alternatively the minimum value (STS-MinIP) along the slab direction depending on the organ or clinical indication, for example, in the lung. The adaptive STS is able to adjust the slab thicknesses depending on the organ of interest and viewing direction and switches between MeanIP, MIP, and MinIP depending on the clinical indication and radiologists’ preferences.

### 2.D. Context-sensitive dual energy evaluation (CSDE)

There are many commercial dual energy applications.<sup>18</sup> The most common material decompositions and classification tasks are realized by almost all (CT) vendors. In this work, we focus on the applications that are implemented by Siemens (italic: official application names in the *Siemens Syngo.CT Dual Energy* software). These dual energy methods rely on two main approaches: firstly, a material decomposition that is used for all kinds of material quantification, and secondly, a material classification that is used for the discrimination and highlighting of two materials. The first method results in two basis material images whereas the second method distinguishes two possible materials that are above or below a certain decision boundary.<sup>19</sup> The methods perform the decomposition and classification in image domain based on the CT value distribution of the low and the high energy image  $f_L$  and  $f_H$  in the DE diagram (see Fig. 2). The low and high energy image span a plane, where the coordinates of any point in the DE diagram is represented by their CT value pair.

Using the dual energy methods, the following applications are realized:

- calculation of pseudomonochromatic images and optimization of the contrast in the images<sup>20</sup> (*Optimum Contrast*, *Monoenergetic* and *Monoenergetic+*).
- material decomposition
  - quantification and color coding of the iodine concentration in the lung<sup>21</sup> (*Lung PBV*) and heart (*Heart PBV*).
  - iodine quantification and virtual noncontrast imaging in the liver (*Liver VNC*) and body

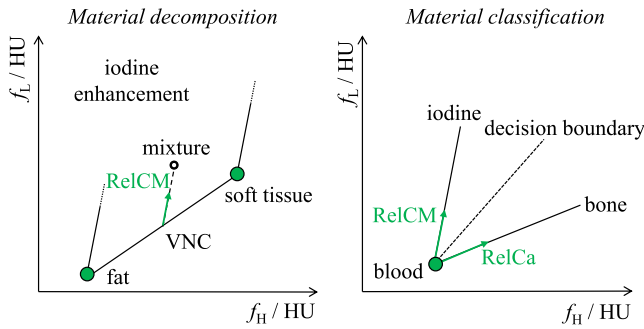


FIG. 2. Dual energy evaluation scheme in image domain. The low- and the high-energy image  $f_L$  and  $f_H$  span a plane where the coordinates of any point in the DE diagram are represented by their CT value pair. Material decomposition: The subtraction of iodine corresponds to a parallel projection onto the virtual noncontrast (VNC) basis line. This line is determined by the position of two reference points, in particular fat and soft tissue for the *LiverVNC* application. RelCM points toward pure iodine and corresponds to the relative iodine contrast in the image. The length of the parallel projection is similar to the iodine concentration of the voxel to be decomposed. Material classification: The differentiation between two materials with known relative contrast in the image (iodine: RelCM and bone: RelCa) is given by their signed distance to the decision boundary.

(*Virtual Unenhanced*) as well as in the brain (*Brain Hemorrhage*).

- subtraction of the calcium content from the bones to display any HU increase due to an infiltration or bone bruising<sup>22</sup> (*Bone Marrow*).
- material classification
  - detection and differentiation between different renal stones (calcium oxalate and uric acid stones)<sup>23–26</sup> (*Calculi Characterization*) or the detection of monosodium urate crystals (gout)<sup>27–29</sup> (*Gout*).
  - removal of  $\text{Ca}^{2+}$  in plaque and bone (*Direct Angio, Hardplaque Display and Bone Removal*)

Each of these applications suffers from the lack of prior anatomical information, performs the dual energy evaluation on the entire dataset, and needs to be invoked by the user. By means of the tissue-related weighting coefficient, the DE application is automatically selected and only applied to the specific organs without any user interaction. This CS analysis allows to simultaneously evaluate multiple organs and to show organ-specific dual energy overlays or tissue classification information wherever appropriate. The method can readily be generalized for other vendors' applications.

### 2.D.1. Automatic patient-specific calibration

In order to obtain a reliable DE analysis, each of the above-mentioned applications needs a patient-specific calibration. The calibration parameters are usually determined by user-defined ROIs. However, the elaborated step of placing these ROIs is often not performed and the default settings are used instead.

A schematic illustration of the algorithms is shown in Fig. 2. The subtraction of iodine corresponds to a parallel projection onto the virtual noncontrast (VNC) line. This line is determined by the position of two reference points, in particular fat and soft tissue for the *LiverVNC* application. RelCM points toward pure iodine and corresponds to the relative iodine contrast in the image.<sup>30</sup> The length of the parallel projection is similar to the iodine concentration of the voxel to be decomposed.<sup>19</sup> However, for a quantitative material decomposition, RelCM as well as the exact position of these reference points must be known, since they determine the slope of the VNC line to which, for example, iodine is to be projected onto.<sup>31</sup> The material classification assumes the knowledge of the exact position of one reference point (blood) as well as the slopes toward the two materials, RelCM for iodine and RelCa for bone<sup>22</sup> in particular, that should be distinguished. The relative contrasts of these two materials with different energy dependency needs to be defined because they determine the slope toward these materials. The slope of the decision boundary is then calculated by averaging the two material-dependent slopes.<sup>19</sup> The final differentiation between these two materials is consequently given by their signed distance to the decision boundary.

The parameter RelCM  $R$  is determined by the DE iodine ratio of the low energy CT value of iodine to the high energy CT value of iodine<sup>30</sup> and is usually in the range of 1.85–3.46 depending on different tube voltage combinations and patient thicknesses.<sup>30</sup> In clinical applications, the default value of this parameter is fixed to 3.01 for the tube voltage combination 80 kV/140 kV + Sn and 2.24 for the tube voltage combination 100 kV/140 kV + Sn. This value might be a good trade-off for most of the patients. However, due to the nonlinearity of beam hardening and scatter, which highly depends on the patients' cross section, the default settings might not be optimal and this may result in an under- or overestimation of the true iodine concentration. Therefore, we believe that an automatic patient-specific calibration improves the iodine quantification accuracy instead of degrading the quantitative capability of the modality. The relative iodine contrast, which defines the slope in the DE diagram, has to be adjusted individually for each patient by means of a calibration.

The relative iodine contrast is defined as the ratio between the differences of the mean values of two ROIs placed within regions of different iodine concentrations acquired at two different energy levels, that is,

$$R = \frac{CT_1(E_L) - CT_2(E_L)}{CT_1(E_H) - CT_2(E_H)}, \quad (7)$$

with  $CT_i(E)$ ,  $i = 1, 2$ , being the ROI's mean value of the measurement at energy level  $E$ . With the unknown mixing ratios  $m_1$  and  $m_2$  of water and iodine, respectively, in these two ROIs, we get

$$CT_i(E) = (1 - m_i)CT_w(E) + m_iCT_1(E), \quad (8)$$

with  $CT_w(E)$  being the CT value of water and  $CT_1(E)$  being the CT value of iodine. Inserting the above Eq. (8) into Eq. (7), it turns out that the unknown mixing ratios cancel out

$$\begin{aligned}
R &= \frac{CT_1(E_L) - CT_W(E_L)}{CT_1(E_H) - CT_W(E_H)} = \frac{CT_1(E_L)}{CT_1(E_H)} \\
&= \frac{\mu_{I,L} - \mu_{W,L}}{\mu_{I,H} - \mu_{W,H}} = \frac{\mu_{I,L} - 1}{\mu_{I,H} - 1}. \quad (9)
\end{aligned}$$

In the second step, we exploit the fact that the CT value of water is zero by calibration. In the third step, the CT values are converted to attenuation values while for the last step, we assume that the values stored in the image are scaled such that  $\mu_W = 1$ . This last convention will be used in the following considerations. Apart from  $R > 1$ , which is true for iodine or other hyperdense materials, please note that

$$R - 1 = \frac{\mu_{I,L} - \mu_{I,H}}{\mu_{I,H} - 1}, \quad (10)$$

$$1 - \frac{1}{R} = \frac{\mu_{I,L} - \mu_{I,H}}{\mu_{I,L} - 1}. \quad (11)$$

We demonstrate in the following the role of the relative contrast ratio  $R$  in the decomposition of the low-energy image  $f_L$  and the high-energy image  $f_H$  into a virtual noncontrast or water image  $f_W$  and an iodine overlay  $f_I$ . The initial images are calibrated such that air is 0 and water is 1. To obtain  $f_W$  and  $f_I$  from two measurements  $f_L$  and  $f_H$ , we make use of the mean values  $\mu_{W,L}$  and  $\mu_{W,H}$  of a water ROI and of the mean values  $\mu_{I,L}$  and  $\mu_{I,H}$  of an iodine ROI, both measured in the low- and high-energy images, to find linear combinations such that

$$1 = c_{W,L}\mu_{W,L} + c_{W,H}\mu_{W,H} \quad (12)$$

$$1 = c_{W,L}\mu_{I,L} + c_{W,H}\mu_{I,H} \quad (13)$$

for the water image (VNC image) and such that

$$0 = c_{I,L}\mu_{W,L} + c_{I,H}\mu_{W,H} \quad (14)$$

$$\gamma = c_{I,L}\mu_{I,L} + c_{I,H}\mu_{I,H} \quad (15)$$

for the iodine image with  $\gamma$  being the value that corresponds to iodine. Exploiting the assumption that  $\mu_{W,L} = \mu_{W,H} = 1$ , we find

$$c_{W,L} = 1 - c_{W,H} = \frac{1 - \mu_{I,H}}{\mu_{I,L} - \mu_{I,H}} = \frac{1}{1 - R} \quad (16)$$

$$c_{I,L} = -c_{I,H} = \frac{\gamma}{\mu_{I,L} - \mu_{I,H}}. \quad (17)$$

The relative iodine contrast is then calculated by the ratio of two ROIs that contain water–iodine mixtures at two energies (ROI in aorta and ROI in liver). The relative calcium contrast is derived in a similar manner<sup>22</sup> by using one ROI in bone and one ROI in fat at two energies. In order to identify the position of the reference points, we evaluate different ROIs in fat, soft tissue, etc. The materials air and water are set to fixed values. Exploiting the prior anatomical information, these ROIs can now be placed automatically into the corresponding anatomical structures.

### 3. RESULTS

#### 3.A. Data acquisition

CT patient data of the chest and the abdomen acquired with a third-generation 128-slice dual source CT system (SOMATOM Definition Flash, Siemens Healthineers, Forchheim, Germany) are retrospectively used in this work. All patients signed written informed consent before the examination. The system operated in dual energy mode, where the x-ray tube voltages were set to 100 and 140 kV, respectively, where the latter operated with a 0.4 mm thick tin prefilter. Iodinated contrast media (CM) (300 mg iodine/mL, Imeron<sup>®</sup> 300 M, Bracco Imaging Deutschland GmbH, Konstanz, Germany) was administered as contrast agent with body weight-adapted volumes. The study was performed for the data of seven contrast-enhanced DECT patient in the arterial and in the portal venous phase. The basis images in the CSR are mixed images  $f_M$  that are calculated by a linear weighting of the DE data

$$f_M(\mathbf{r}) = (1 - \delta)f_L(\mathbf{r}) + \delta f_H(\mathbf{r}). \quad (18)$$

The mixing weight  $\delta$  is set to 0.5 as preset at our system. The resulting images yield the same noise and contrast enhancement properties compared to a dose-equivalent single-energy CT scan at 120 kV.<sup>19</sup>

#### 3.B. Prior anatomical information

The multiorgan segmentation is obtained using the previously mentioned cascaded 3D fully connected CNN.<sup>6</sup> Currently, this method is limited to large organs like the liver, left and right kidney, spleen, aorta, and left and right lungs. The CNN robustly segments the listed anatomical regions also in the presence of high image noise. Since the network has never seen images highly degraded by artifacts during training, it may fail on such unseen data during inference. In this work, we therefore excluded heavily degraded images primarily due to such images being absent in our data. Moreover, the remaining yet unlabeled voxels are assigned to one tissue class using a naive threshold-based segmentation. The thresholds are selected using Otsu's method.<sup>11</sup> The CT value distribution ambiguities between the vascular system and bone result in misclassification of the two tissue classes. We therefore need to manually refine the class boundaries between iodinated tissue and bone by manually removing misclassified voxels from the masks. Overall, the total number of class labels is currently restricted to  $L = 9$ , consisting of bone, lung, liver, kidneys, spleen, aorta, vasculature (including heart and large vessels), muscles, and fat. The lung mask also includes the trachea as well as the bronchial tree. Furthermore, in order to account for ambiguities between adjacent tissue labels, we solve for smooth tissue-related weighting coefficients that are utilized in the CS CT imaging. These weights are defined according to Eq. (1) and derived from the binary masks as shown in Fig. 3. The tissue-related weights introduce artificial overlapping areas between adjacent tissue

classes. A transition zone diameter controls the width of the overlap.

### 3.C. CSD

#### 3.C.1. Context-sensitive spatial resolution

The tissue-related weights guide the weighted sum of involved basis images in the CSR. In order to analyze the influence of the tissue-related weights, a line profile in the CSR image (see Fig. 4 left) is drawn through the lung, bone and soft tissue consisting of muscles as well as fat.

The position of the profile is chosen such that it traverses four tissue classes. The considered tissue-related weight masks (with highlighted profile indicated by arrows) are also illustrated in Fig. 3. The line profile along the tissue-related masks is shown on the right in Fig. 4. Each of these profiles reflect the contribution of the corresponding involved tissue-related weight. Therefore, each voxel along the profile is composed of the assigned basis image weighted by their tissue-related coefficient. Since each of these weights is assigned to one basis image, it determines the contribution of that specific basis image in the transition area of adjacent tissue labels.

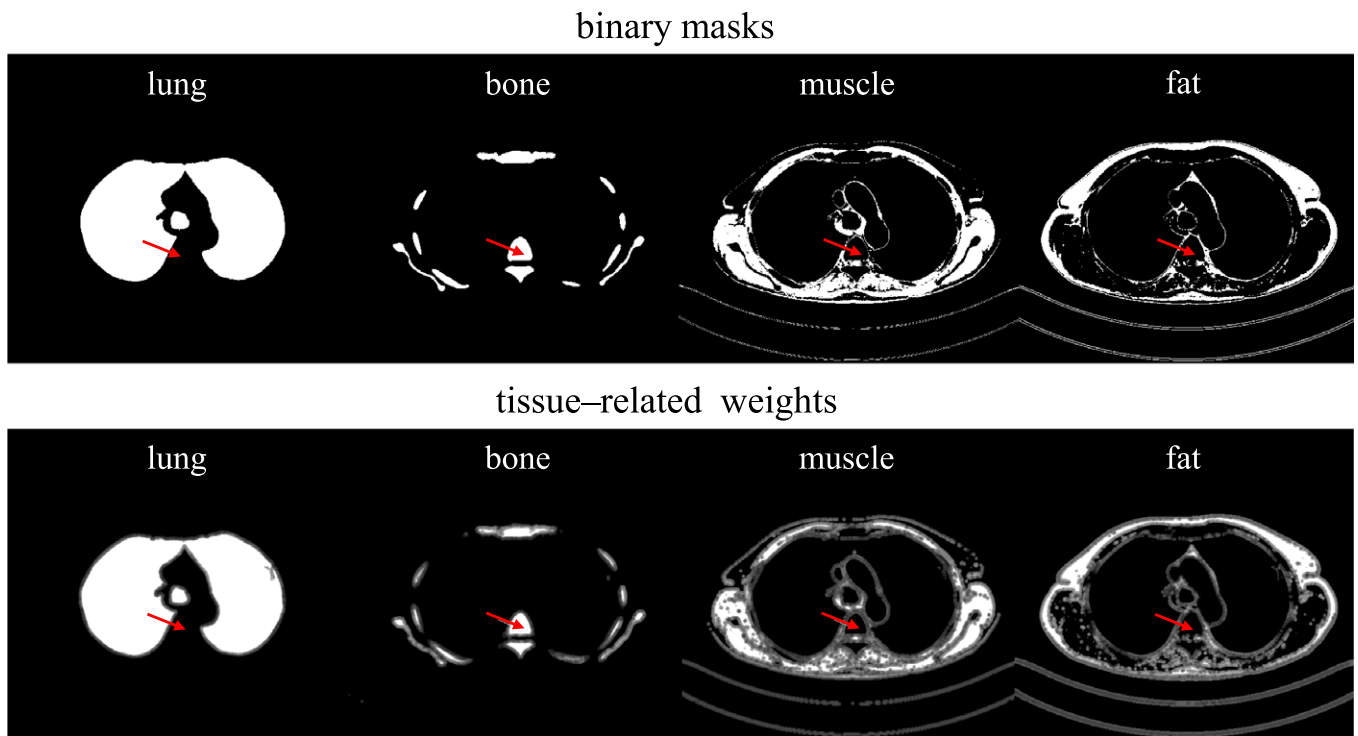


FIG. 3. Binary masks of anatomical structures that are generated using the automatic segmentation as well as the tissue-related weights to cope with the boundaries of adjacent structures. The weights are normalized in order to yield a convex combination. The arrows correspond to the position of the line profile in Fig. 4.

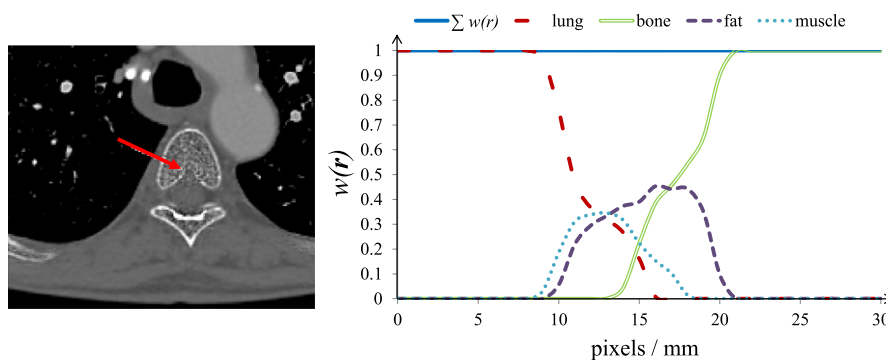


FIG. 4. Left: line profile traversing four tissue types lung, muscle, fat, and bone to illustrate the contributions of the tissue-related weights and associated basis images in the CSR. Right: the contribution of the tissue-related weights during the CSR along the line profile through the lung, bone, muscle, and fat. The pixels are compounded using a weighted sum of the associated basis images. The tissue-related weight determines the contribution of each basis image in the transition area of adjacent tissue labels.

We compare a conventionally reconstructed smooth basis image  $f_{\text{smooth}}$  and sharp basis image  $f_{\text{sharp}}$  with the associated CSR image  $f_{\text{CSR}}$  in Fig. 5. In this setup, we chose the number of basis images  $B = 2$  and the smooth basis image  $f_{\text{smooth}}$  denotes a reconstruction with the D20f kernel and the sharp basis image  $f_{\text{sharp}}$  denotes a reconstruction with the B80f kernel. The image is composed of the smooth basis image for soft tissue, fat, organs etc., and sharp basis image for lung and bone revealing no information loss. In order to highlight the advantages of the compound image, piecewise magnifications are shown in three typical window level settings, namely the body window, lung window, and bone window. The CSR image yields a significantly higher spatial resolution in high contrast objects like the lung or bone while maintaining a low noise level in the soft tissue compared to the basis images. The evaluation of two ROIs as well as a line profile that is drawn through the lung and heart and a line profile that is drawn through the lung, bone, and soft tissue in both basis images and in the CSR image confirms this result (see Fig. 6).

The number of basis images can be further increased in order to obtain a better adaption to different anatomical structures. There are many analytic reconstructions that are adapted to different anatomical regions. For instance, a B23f kernel also includes a beam-hardening correction for iodine and is often recommended for a reconstruction of the vascular system.

### 3.C.2. Influence of transition zone diameter

The transition zone diameter that is used to calculate the tissue-related weight for the CSR has a strong impact on the boundaries of adjacent tissue classes in the CSR image. The diameter  $d$  strongly depends on the segmentation accuracy, because it determines the width of the weighted average calculation. Wherever one of the weights is within the interval of 0 and 1, more than one basis image contribute to the CSR image. The influence of the diameter of the transition zone is depicted in Fig. 7. It shows an image section of the borders between anatomical structures that are composed of competing basis images, in particular, the boundary between lung and soft tissue as well as the boundary between soft tissue and bone. If no transition zone is used, that is, the diameter is set to  $d = 0$  mm, a bright overshoot appears at the border between lung and soft tissue. Voxels that should result from a smooth basis image result from a sharp basis image. The volume of the binary lung mask is slightly too large, and therefore, the voxels are incorrectly assigned to the lung mask at the boundaries of the organ. On the other hand, a large transition zone diameter (e.g.,  $d = 6$  mm) reduces the spatial resolution of the bone because of an averaging of the sharp basis image in the bone with the smooth basis image of the surrounding. The same effect also appears at the boundaries between lung

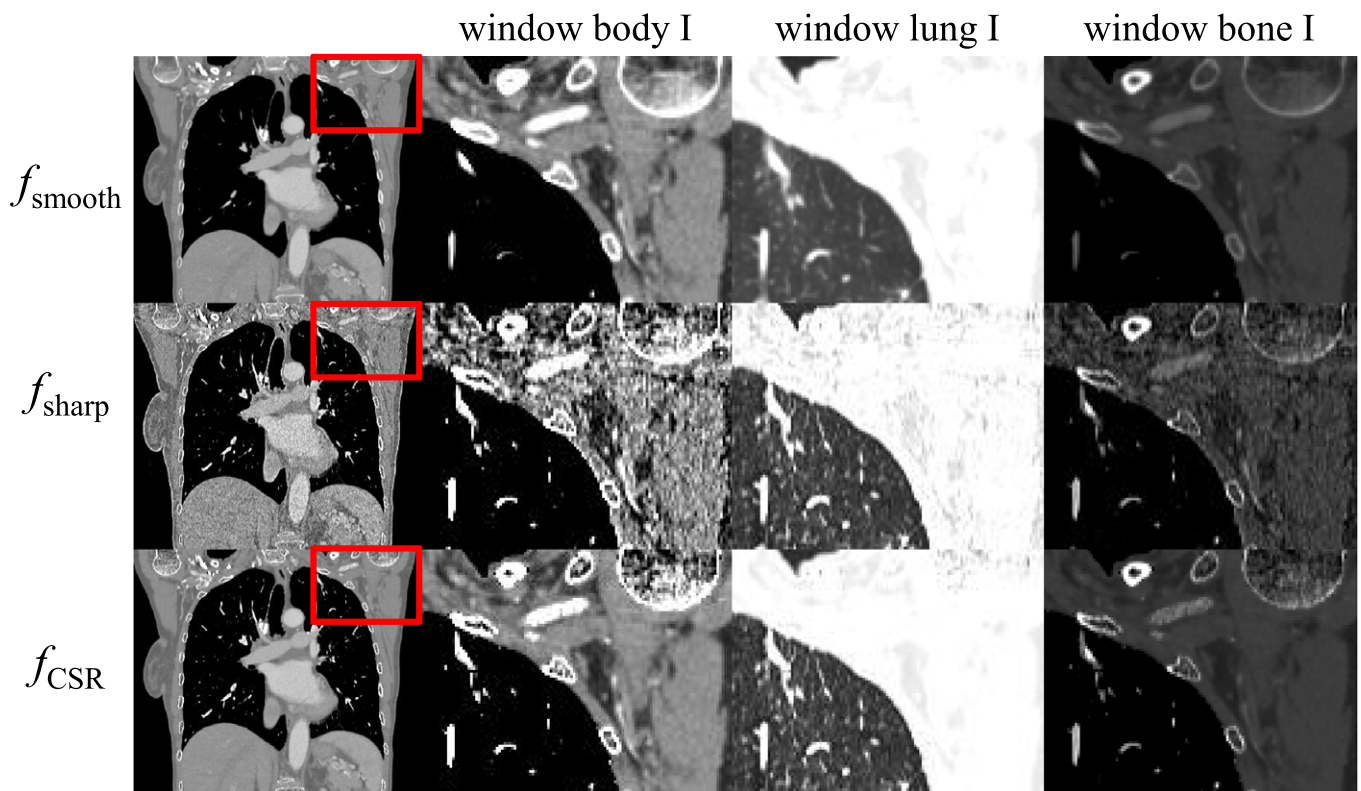


FIG. 5. Patient C. Comparison between the smooth basis image  $f_{\text{smooth}}$ , the sharp basis image  $f_{\text{sharp}}$ , and the CSR image  $f_{\text{CSR}}$  in three different window level settings (soft tissue, lung, and bone window). The CSR image combines the advantages of both basis images: a high spatial resolution in high contrast areas, for instance the lung and bone, and a low noise level in soft tissue.

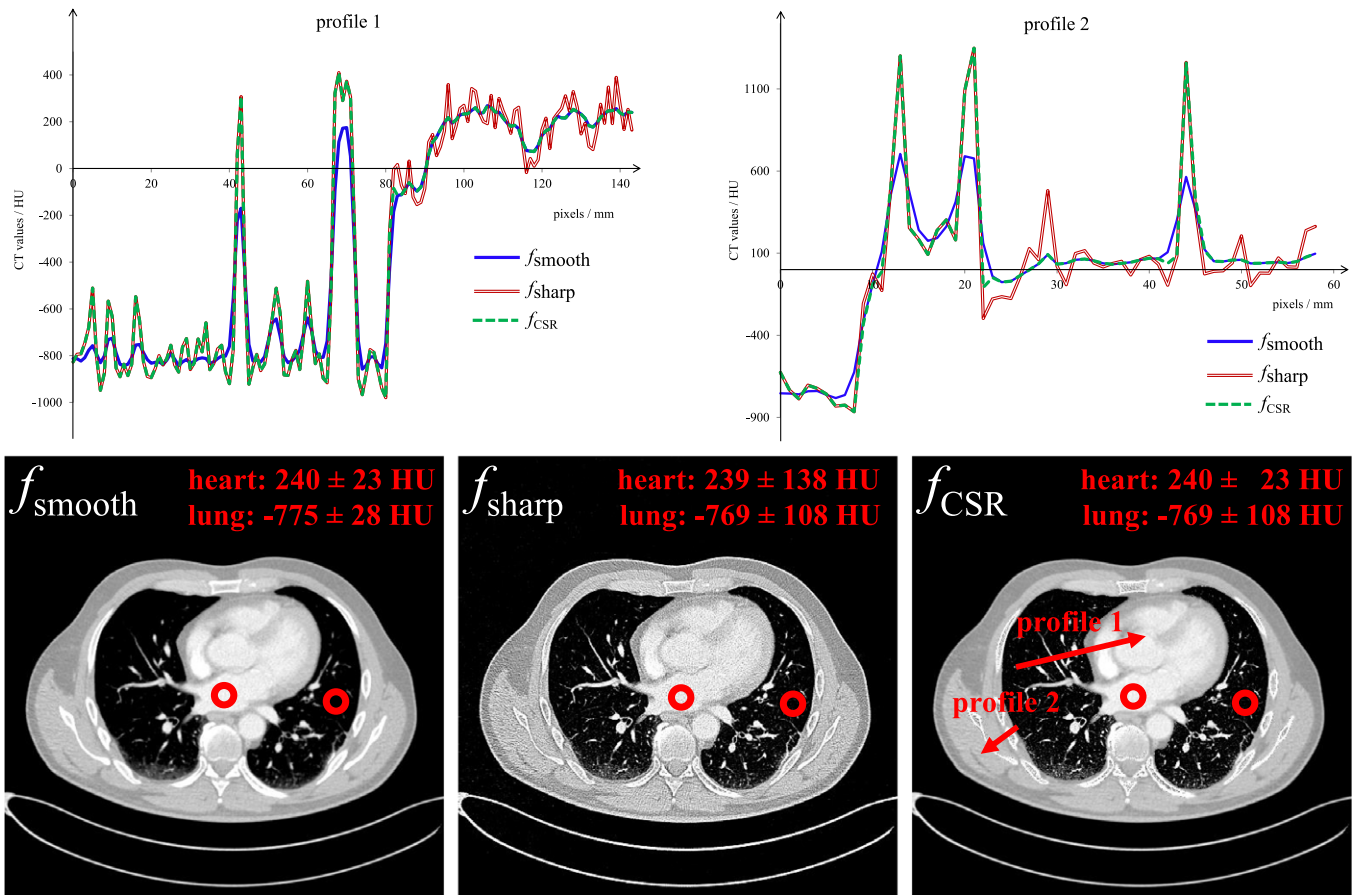


FIG. 6. Line profiles taken from the both basis image  $f_{smooth}$  and  $f_{sharp}$  as well as from the corresponding CSR image ( $C = -200$  HU,  $W = 1000$  HU) through the lung and the heart (profile 1) and through the lung, bone, and soft tissue (profile 2). Two ROIs in the lung and heart are further evaluated regarding the noise level and spatial resolution.

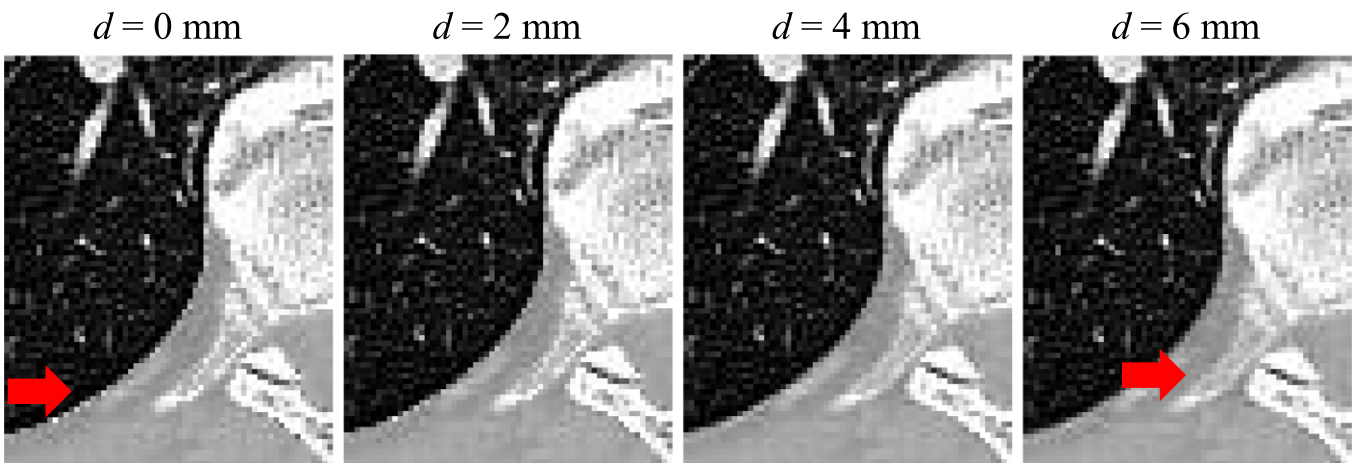


FIG. 7. Influence of transition zone diameter during the CSR. From left to right ( $C = -200$  HU,  $W = 1500$  HU): if there is no transition zone used ( $d = 0$  mm), the border between lung and soft tissue (muscle and fat) shows a bright streak. The adjacent soft tissue also results from a sharp basis image because the volume of the binary lung mask is slightly too large and voxels are incorrectly assigned to the lung. A large transition zone diameter (e.g.,  $d = 6$  mm) leads to a smoothing of the sharp kernel reconstruction in the bone. A transition zone diameter  $d = 4$  mm results in a good compromise in the transition zone.

and soft tissue. A transition zone diameter of  $d = 4$  mm results in a good trade-off between hard transitions and the loss of spatial resolution due to the averaging of

adjacent basis image reconstructions. Since all datasets are segmented with the same segmentation approach, the diameter is empirically determined to 4 mm in the CSR.

### 3.C.3 Adaptive window level settings and STS

In clinical practice, there are many predefined window settings for different anatomical structures available that are used for daily diagnosis. Table I lists typical window level settings for varying organ windows, as they could be preset by default on a clinical CT device. However, within a single given gray level window, the full information contained in the CSR image cannot be adequately visualized as we have seen in Fig. 5 (soft tissue window I vs lung window I vs bone window I).

The adaptive windowing approach solves this problem by locally adjusting the window level settings for each organ separately. Figure 8 demonstrates that a CSR image with the use of a sophisticated adaptive CS windowing presents significantly more information to the reader compared to both basis images and to the CSR image in one specific window level setting, for instance the body window I. The different CS window level settings are listed in Table II. The settings of CS window I and CS window II differ only in the gray level window settings of the lung and may be adjusted to a desired visual perception. The vascular system, including the aorta and the heart, is windowed with an angiography window. This window reduces the bright iodine contrast in particular in the heart and aorta. The liver window is narrower than the applied body window I in order to improve the soft tissue contrast and therefore to highlight the liver vessels. The third CS window III aims at maximizing the visual contrast while maintaining the conventional image impression. We therefore chose a wider window for the bone (bone II) and a darker window for the lung (lung III). The center of the soft tissue window is also slightly translated to a higher CT value. In a clinical application, the center and the width for each organ, respectively, are interactively adjustable on demand.

To reduce the noise in the soft tissue, an STS-MeanIP in these areas is used. Moreover, in order to highlight the parenchyma, an STS-MIP in the lung is applied to the data. Figure 9 illustrates the overall CSD display of three patient datasets. For this data presentation, the transition diameter is set to 4 mm and the blending diameter, which will be discussed in the following section, is set to 2 mm. The slab

thickness of the STS-MeanIP is set to 5 mm in the soft tissue and different organs. The value is selected since it reduces the noise level to a sufficient level. Furthermore, we use a slab thickness of 10 mm for the STS-MIP display. The data are windowed with the CS window III. While in the conventional STS technique, the entire dataset is processed, we reduce the corresponding display to the essential anatomical structures. Thus, one can examine several anatomical structures simultaneously.

### 3.C.4 Influence of blending diameter

We establish a smooth blending between adjacent window level settings. The size of the blending area is determined by the blending diameter that is used to calculate the tissue-related weights corresponding to the CSR. These recalculated weights are then utilized in the CSD. The influence of the blending diameter is illustrated in Fig. 10. If no blending ( $d = 0$  mm) is performed, hard transitions between adjacent windows arise. However, if the blending diameter is too large, dark areas around the lung arise, since the soft tissue window contributes to the lung windows. The CT values that are mapped to black in the soft tissue window are no longer mapped to black in the lung window. The dark areas could be misinterpreted as pneumothorax and therefore should be avoided. The larger the blending diameter, the wider the dark area in the transition between lung and soft tissue is. There is a trade-off between the selection of tissue-related window level settings and the selection of a proper blending diameter. Therefore, the blending diameters must be assessed depending on the visual perception and freely specifiable to the user. Overall, in our experiments, a blending diameter of 2 mm results in a satisfying compromise.

## 3.D. CSDE

Figure 11 shows an overview of the CSDE evaluation and analysis. The mixed image  $f_M$  is used as background for the color overlays of the various DE applications. We first perform a set of iodine quantifications, that is, a lung perfused blood volume (PBV), a liver iodine quantification, and a body iodine quantification. The liver and body iodine quantifications differ by their slope of the VNC baseline in the DE diagram. The liver iodine quantification is optimized for that specific organ. Voxels inside the liver are assumed to be a composition of the two reference materials, fat and soft tissue, and iodine. The body iodine quantification uses water and air as reference point that results in a VNC line with a slope of 1. The decomposition is not optimized for a specific organ. Each of these applications is now invoked only for the specific organ and the iodine content is overlaid with different color codings. The DE is extended to accomplish two competing DE evaluations of the bone. We indicate either a bone marrow analysis that color codes any HU increase due to an infiltration or bone bruising or a bone removal. Within one single DE image, we combine material decomposition

TABLE I. Window level settings used in the CSD.

Anatomical structure	Window settings	
	Center (HU)	Width (HU)
Body I	30	400
Body II	60	400
Liver	40	200
Heart	200	600
Angiography	100	900
Bone I	450	1500
Bone II	300	2000
Lung I	-600	1200
Lung II	-600	1600
Lung III	-400	1400

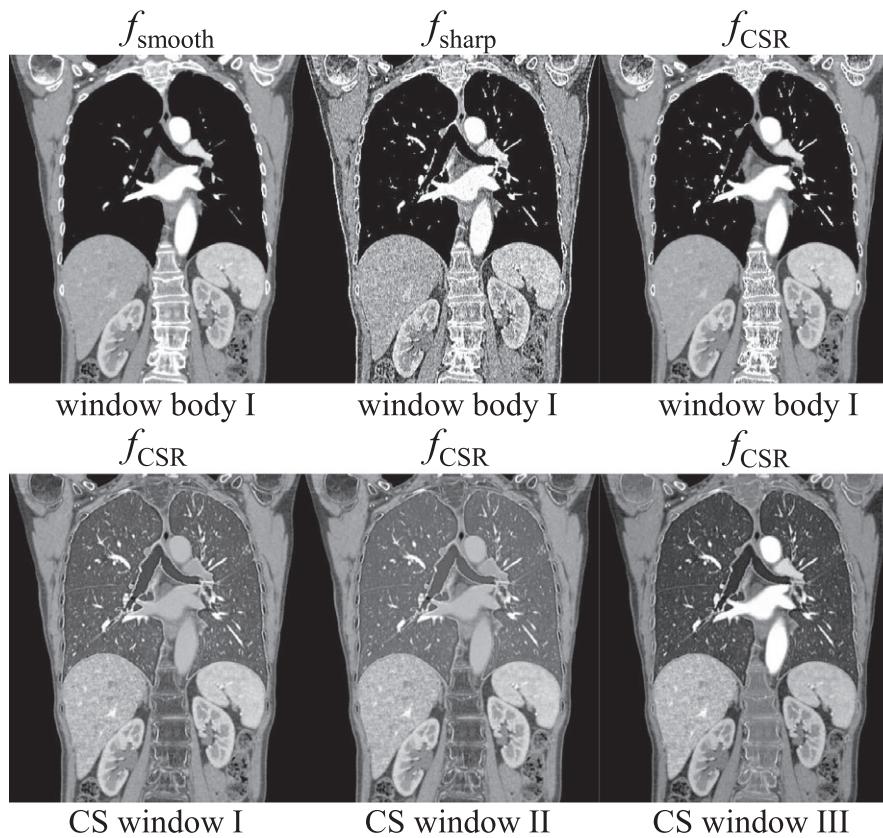


FIG. 8. First row from left to right: smooth basis image, sharp basis image, and CSR image displayed in the body window I. Second row from left to right: the CSR shown with adaptive window settings CS window I, CS window II, and CS window III. The (CSD) settings are summarized in Table II.

TABLE II. Exemplary CS window settings.

	Anatomical structure				
	Lung	Bone	Vasculature	Soft tissue	Liver
CS window I	Lung I	Bone I	Angiography	Body I	Liver
CS window II	Lung II	Bone I	Angiography	Body I	Liver
CS window III	Lung III	Bone II	Body II	Body II	Liver

and classification tasks and are able to show color overlays wherever appropriate.

Evermore applications can be applied to a restricted body region. Figure 11 shows only a selection of possible evaluations and an interactive activation or deactivation of specific applications as well as the changeover to a conventional DE display is always possible.

### 3.D.1. Automatic patient-specific calibration

A direct comparison between the default calibration and an automatic calibration of the patient-specific parameters is shown in Fig. 12 for Patient A. The color overlays show nearly identical iodine distributions compared to those obtained by using the default calibration. A quantitative evaluation of the iodine content in five ROIs leads to a root mean square error of 0.095 mg/mL for this patient. The mean

values of the iodine content in five ROIs that are placed in different anatomical structures, that is, aorta, lung, spleen, kidney and liver, for overall six patients are listed in Table III. The ROIs are drawn with similar size and position in each of the evaluated patients A–F. Since no ground truth is available, we assume that the default calibration is a good trade-off and provides accurate iodine concentrations. Therefore, those values are used as reference iodine concentrations to evaluate the automatic patient-specific calibration. The mean relative error per patient is chosen as an estimate of the overall deviation between the iodine concentrations obtained with the default calibration  $c_{\text{default}}$  and the iodine concentrations obtained with the automatic patient-specific calibration  $c_{\text{patient}}$ .

$$e_{\text{patient}} = \frac{1}{N} \sum_{n=1}^N \frac{|c_{\text{default},n} - c_{\text{patient},n}|}{c_{\text{default},n}}, \quad (19)$$

where  $N$  is the total number of evaluated ROIs. Furthermore, we evaluate the root-mean-square error per patient

$$\text{RMSE}_{\text{patient}} = \sqrt{\frac{1}{N} \sum_{n=1}^N (c_{\text{default},n} - c_{\text{patient},n})^2}. \quad (20)$$

The automatic patient-specific calibration yields iodine concentrations which are in accordance with the iodine concentrations obtained with the default calibration. Table IV summarizes the adapted relative iodine contrast

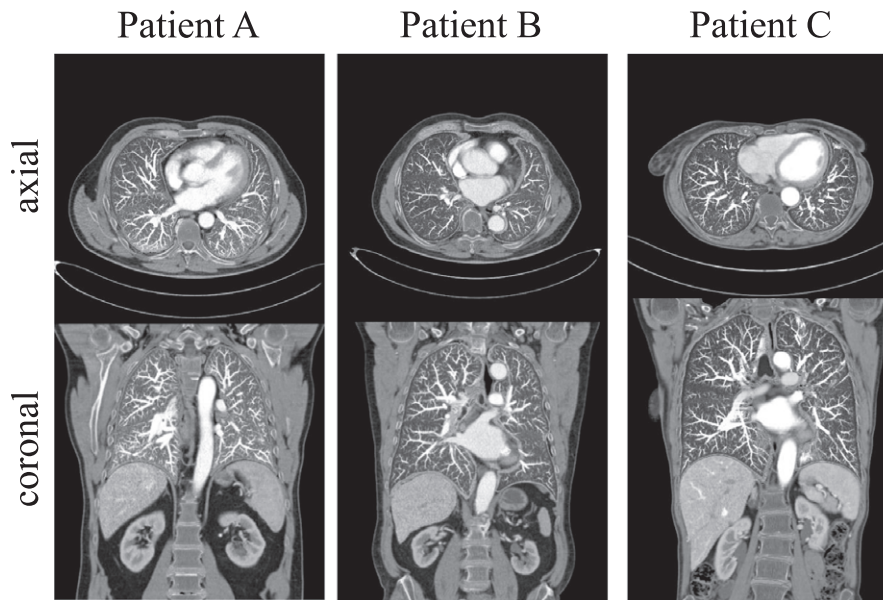


FIG. 9. STS-MeanIP in soft tissue over 5 mm and STS-MIP in the lung over 10 mm for three patient datasets. The transition diameter is set to 4 mm and the blending diameter is set to 2 mm.



FIG. 10. Different blending diameters. No blending leads to hard transitions between adjacent windows. However, if the blending diameter is too large, dark areas around the lung arise, since the soft tissue window contributes to the lung windows. CT values that are mapped to black in the soft tissue window are not mapped to black in the lung window. A blending diameter of 2 mm results in a satisfying trade-off. The larger the blending diameter the darker is the transition between lung and soft tissue.

$R$  per patient, the patient-specific mean relative error, and the root-mean-square error. It should be noted that the last row of this table represents the mean and standard deviation of the overall relative iodine contrast  $R$ , the overall mean relative error  $e$ , and the RMSE over all patients. The automatic patient-specific calibration yields an overall mean relative error of  $3.04 \pm 1.26\%$  that corresponds to an overall RMSE of  $0.16 \pm 0.08$  mg/mL. These deviations result from the adaptation of the relative contrast media  $R$  to the actual patient size. The patient-specific calibration, which delivered values ranging from 2.132 to 2.227 depending on the patient, therefore compensates for beam hardening and scatter.

#### 4. DISCUSSION AND CONCLUSIONS

In this paper, we propose a new paradigm to combine mutually exclusive image properties, which result from different reconstruction algorithms, display settings and dual energy evaluations, into a single CS imaging by exploiting prior anatomical information. The incorporation of prior knowledge, which is gained from an automatic multiorgan segmentation, enables the combination of various desired characteristics into a single CS image generation and presentation. Furthermore, by using the prior anatomical information, numerous DECT applications as well as any other evaluation methods can be combined into one single tool.

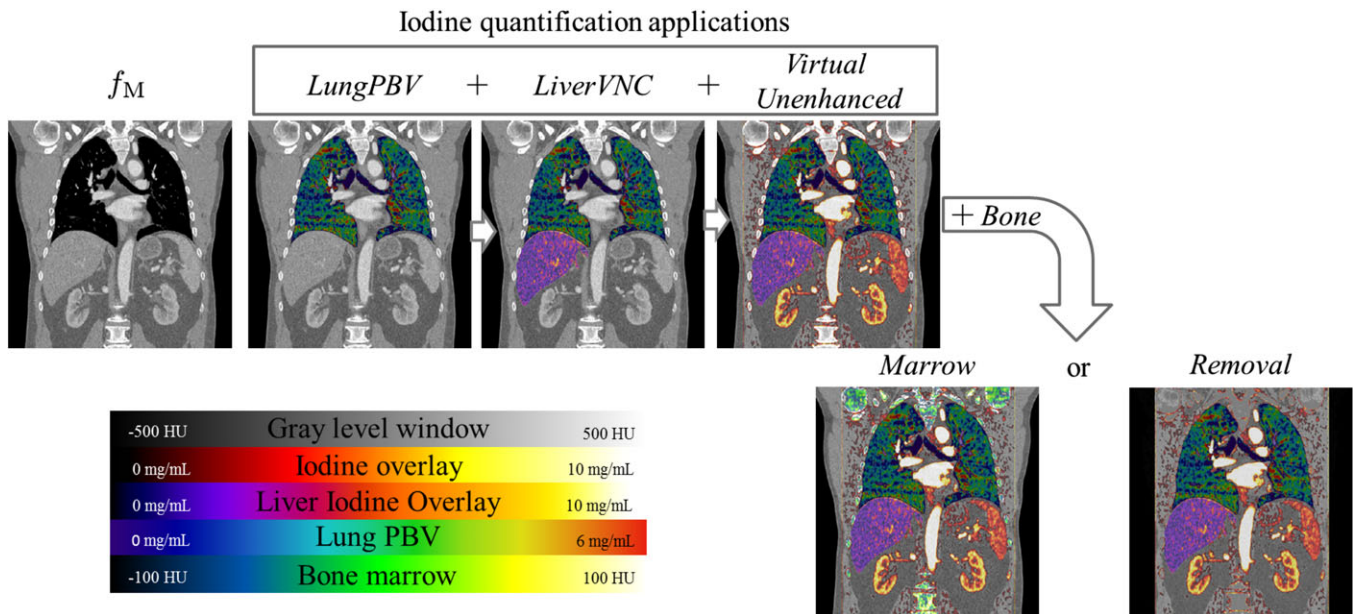


FIG. 11. Context-sensitive dual energy evaluation scheme. Each of the applications is automatically invoked and applied to the organ of interest.

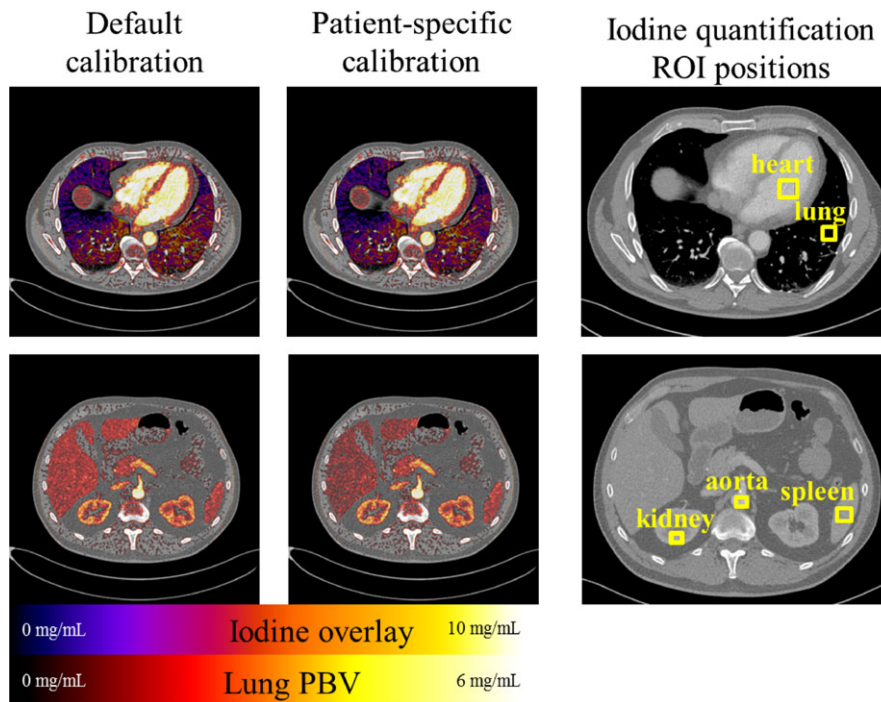


FIG. 12. Iodine quantification accuracy of the automatic calibration. The color overlay of three invoked quantification algorithms (liver iodine map (*LiverVNC*), perfused blood volume in the lung (*LungPBV*), body iodine map (*Virtual Unenhanced*)) is shown at two different  $z$  positions. The iodine content is further evaluated in the ROIs delineated in red in the right column.

Based on the CS information, the tools can be chosen and applied to the different organs simultaneously. Instead of having one single manually selected dual energy evaluation, the prior-based DE scheme performs all organ-specific feasible methods at once.

The multiorgan segmentation, which is based on a cascaded 3D fully connected CNN,<sup>6</sup> enables us to do

context-sensitive imaging. We assume that an accurate multi-organ segmentation is available that allows for the automatic labeling of organs in CT data. Our primary focus of this work is the presentation of the novel paradigm of CS CT imaging and how CT imaging in general might benefit from an ideal segmentation. Therefore, the presented method is not restricted to this specific CNN approach and might as well be

TABLE III. Evaluation of the mean iodine concentration  $c_{\text{default}}$  and  $c_{\text{patient}}$  in different anatomical structures for six example patients. The corresponding ROIs of example Patient A are shown in Fig. 12. Please note that comparable ROIs are evaluated with similar size and position in all patients.

	Patient A		Patient B		Patient C	
	$c_{\text{default}}$ (mg/mL)	$c_{\text{patient}}$ (mg/mL)	$c_{\text{default}}$ (mg/mL)	$c_{\text{patient}}$ (mg/mL)	$c_{\text{default}}$ (mg/mL)	$c_{\text{patient}}$ (mg/mL)
Aorta	9.92	9.97	13.43	13.12	8.63	9.14
Heart	9.23	9.33	11.52	11.27	7.27	7.70
Spleen	2.61	2.67	4.57	4.47	2.12	2.24
Kidney	4.85	4.90	5.97	5.84	3.84	4.06
Lung	1.81	1.65	1.39	1.27	1.52	1.59

	Patient D		Patient E		Patient F	
	$c_{\text{default}}$ (mg/mL)	$c_{\text{patient}}$ (mg/mL)	$c_{\text{default}}$ (mg/mL)	$c_{\text{patient}}$ (mg/mL)	$c_{\text{default}}$ (mg/mL)	$c_{\text{patient}}$ (mg/mL)
Aorta	9.31	9.38	9.51	9.74	9.08	9.23
Heart	9.51	9.58	8.92	9.13	11.44	11.63
Spleen	3.20	3.22	2.32	2.38	2.84	2.89
Kidney	4.79	4.83	5.74	5.87	4.97	5.05
Lung	2.11	1.97	2.06	2.15	2.00	2.04

TABLE IV. Patient-specific relative iodine contrast, corresponding mean relative error, and root-mean-square error between measured iodine concentrations resulting from default vs automatic calibration of the six example patients. Please note that the last row represents the mean and standard deviation of the overall patient-specific relative iodine contrast  $R_{\text{patient}}$ , the overall  $e_{\text{patient}}$  and overall  $\text{RMSE}_{\text{patient}}$ .

Patient	$R_{\text{patient}}$	$e_{\text{patient}}(\%)$	$\text{RMSE}_{\text{patient}}$ (mg/mL)
A	2.226	2.79	0.095
B	2.227	3.50	0.20
C	2.132	5.54	0.32
D	2.145	1.92	0.079
E	2.194	2.76	0.16
F	2.206	1.74	0.12
overall $\mu \pm \sigma$	$2.188 \pm 0.037$	$3.04 \pm 1.26$	$0.16 \pm 0.08$

replaced by other suitable segmentation approaches, for example, probabilistic atlas-based methods.<sup>32–36</sup>

In order to account for small inaccuracies in the automatic segmentation and ambiguities at organ boundaries, smooth tissue-related weights are introduced. In this paper, we chose constant diameters for the calculation of the transition weights. The optimal diameter for the transition zone in the image composition turns out to be 4 mm and the blending diameter in the organ-adapted window is set to 2 mm. These values provide in our experiments a qualitative superior image impression. We assume that in comparison to most clinical relevant pathologies, these diameters are very small. Furthermore, since some organ-specific window level settings are more similar to adjacent windows than others, the weights could also be varied across different anatomical structures using adaptive transition zone diameters. Future work could also include the replacement of the tissue-related weights with a probabilistic atlas or the output probabilities of the neural network-based segmentation. Moreover, we need to

mention that the segmentation is still a work in progress, which will constantly be improved. Furthermore, we are hoping that the current neural network-based segmentation will be extended to segment more and more anatomical structures. To do this, the network should be retrained with the associated ground truth segmentations of these target structures, which must be provided by medical experts. As a consequence, we are expecting to overcome the threshold-based segmentation and manual correction step in the near future.

Overall, there is considerable potential in exploiting prior anatomical information for CT imaging. The CS image combines indication-specific advantages of different parameter settings. Each tissue type is displayed with the clinically most appropriate reconstruction algorithm (here: kernel). The CSR provides images with low noise while maintaining high spatial resolution in air and highly attenuating materials by choosing the best-adapted basis image during the image composition on a per-voxel basis. The CSR image, therefore, combines the advantages of different reconstructions. The CS images are composed of quantitative CT basis images, and therefore, the CT values themselves in the compound image are not altered or lost in any case. Since the CT values during image formation and display do not change, we expect no loss in the quantitative capability of CT. The number of necessary images to present to the radiologists may hence be reduced to one CSR. Furthermore, we demonstrate that the CSD is able to combine the advantages of different window level settings into one adaptive CS window. Moreover, the CSD enables the reduction of the remaining noise level in different anatomical structures by viewing specific organs in thicker slabs. The adaptive STS technique further performs a MIP, for example, of the lung simultaneously. The number of images to display might also be reduced to one CSD image since our proposed display method outperforms the conventional image viewing. It highlights each anatomical structure by applying best organ-related display settings and therefore

increases the amount of visible information in the CT image. The proposed display method provides high quality images, which achieve an improved image impression. The automatic DE calibration yields accurate material decompositions and classifications by means of prior anatomical knowledge. Exploiting this available information allows us to automatically calibrate, select, and apply an organ-dependent DE evaluation method. Hence, we establish a simultaneous evaluation and analysis of various DE applications without the need of any user interaction. In particular, the automatic patient-specific calibration of the relative iodine contrast might be a conceivable improvement of the iodine quantification accuracy, since the default calibration neglects the actual patient size. The resulting CSDE image combines and highlights the contributions of different material decompositions and classifications and therefore assigns the spectral information as third dimension to the CS imaging. The method is not restricted to DE data and can readily be generalized to the cases of multienergy CT data as well as to other modalities.

However, there is a notable parameter issue. In CS imaging, there are a lot of parametric choices to be made. On the one hand, there are the existing parameters that have a strong impact on the resulting CS image, its display and analysis. On the other hand, there are newly introduced parameters, which are needed to actually perform the CS imaging, particularly the width of the tissue-related weight that determines the overlap between adjacent anatomical structures. In order to calculate a CSR image, the number and type of the basis images must be determined. The basis image can be reconstructed either iteratively or analytically. In particular, for analytic reconstructions, there are a great variety of convolution kernels, each resulting in different image properties regarding the noise level and spatial resolution. We currently have no clinical experience regarding our proposed method. However, different institutions and different physicians may have their own preferences regarding the kernels and their usage. Thus, the kernel selection and the kernel-to-organ assignment would be freely specifiable by the user. While two kernels are the absolute minimum, it may well be the case that users prefer to see significantly more than two kernels. Depending on the implementation, processing time is not really an issue because often the images can be generated by applying the shift invariant parts of the kernel to a single master image, and it thus requires just a single reconstruction. In our examples, we used the scanner's reconstruction which does not provide us with such a master image and had to carry out one reconstruction for each kernel. Once a CS image is composed, display parameters need to be determined: the window level settings for each organ, the organ-specific STS technique as well as the corresponding slab thicknesses for each of them. Beside the presented context-sensitive display approaches, the principle could also be extended to any other display technique. The next step is to decide which DE evaluation method should be applied to which organ. For some organs, there is more than one DE evaluation (*Bone Marrow vs Bone Removal*) reasonable, and therefore, a decision needs to be made. The evaluation method and how to best present

the data to the radiologist (color overlays, pop-up menus, volume rendering, etc.) is also an issue. In consultations with radiologists and medical experts as well as after comprehensively reviewing state-of-the-art literature, we have identified and agreed upon the selection of the kernels and number of basis images, the common display settings as well as number and type of applied DE evaluation methods. Both diameters of the transition or blending zone, respectively, are selected such that the image appearance is optimal. This paper provides only a proposal on the parameter selection and could be extended or changed without restriction of any kind. In conclusion, we propose to display only one single CS image to the radiologists whereby the default parameter selection could be regarded as a recommendation. The interactive tuning takes place in this CS image presentation.

This paper offers a proof of concept to demonstrate the feasibility and potential benefit of CS imaging. But currently, the radiologists are not aware of the CS images and the veritable diagnostic reliability of them has not yet been clinically evaluated. Therefore, in order to perform an extensive clinical study, a graphical user interface (GUI) is required that could be handed to the radiologists. This GUI should contain the variety of the most popular functionalities as well as our novel methodology. Using the GUI, the parameters can be adjusted for each organ individually. For instance, the user might be able to change the window level settings for one organ separately while keeping the window level settings for the other organs constant to a preset window. We are currently developing a basic GUI in order to integrate the CS imaging into the clinical routine. Using this GUI, the radiologist will experience the novel technique and will be able to modify different parameters. Future work will include a comprehensive clinical evaluation to analyze the diagnostic potential of the CS imaging.

In summary, this new paradigm is a potential step toward presenting evermore increasing complex information in CT and toward improving the radiologists' workflow significantly. During case discussions and presentations, the switching between different image stacks may no longer be necessary since the CS image combines the advantages of varying reconstructions and display settings. DE color overlays could be dynamically superimposed in order to present an additional quantitative analysis to the radiologist. The combination of varying DE applications might assist the radiologist to find a precise diagnosis. CS imaging could increase diagnostic accuracy by improving the sensitivity for incidental findings, for example, small nodules can be diagnosed in the lung parenchyma even if the main focus of the radiologist was assessing the soft tissue.

## ACKNOWLEDGMENTS

This work was supported by the Deutsche Forschungsgemeinschaft (DFG) under grant KA 1678/20-1, LE 2763/2-1 and MA 4898/5-1. Parts of the reconstruction software were provided by RayConStruct<sup>®</sup> GmbH, Nürnberg, Germany.

## CONFLICT OF INTEREST

The authors have no conflicts of interest to disclose.

<sup>a)</sup> Author to whom correspondence should be addressed. Electronic mail: [sabrina.dorn@dkfz.de](mailto:sabrina.dorn@dkfz.de); [www.dkfz.de/ct](http://www.dkfz.de/ct).

## REFERENCES

- Hofmann C, Sawall S, Knaup M, Kachelrieß M. Alpha image reconstruction (AIR): a new iterative CT image reconstruction approach using voxel-wise alpha blending. *Med Phys*. 2014;41:061914–1–061914–14.
- Harris KM, Adam H, Lloyd DCF, Harvey DJ. The effect on apparent size of simulated pulmonary nodules of using three standard CT window settings. *Clin Radiol*. 1993;47:241–244.
- Pomerantz SM, White CS, Krebs TL, et al. Liver and bone window settings for soft-copy interpretation of chest and abdominal CT. *Am J Radiol*. 2000;174:311–314.
- Ertl-Wagner B, Bruening R, Blume J, et al. Relative value of sliding-thin-slab multiplanar reformations and sliding-thin-slab maximum intensity projections as reformatting techniques in multisection CT angiography of the cervicocranial vessels. *Am J Neuroradiol*. 2006;27:107–113.
- Napel S, Rubin GD, Jeffrey RBJ. STS-MIP: a new reconstruction technique for CT of the chest. *J Comput Assist Tomogr*. 1993;17:832–838.
- Chen S, Roth H, Dorn S, et al. Towards automatic abdominal multi-organ segmentation in dual energy CT using cascaded 3D fully convolutional network. In: *Proceedings of the Fifth International Conference on Image Formation in X-Ray Computed Tomography*. Salt Lake City: Utah Center For Advanced Imaging Research (UCAIR); 2018:395–398.
- Ronneberger O, Fischer P, Brox T. U-Net: convolutional networks for biomedical image segmentation. In: *Medical Image Computing and Computer-Assisted Intervention – MICCAI*. 2015: 18th International Conference, Munich, Germany, October 5–9, 2015, Proceedings, Berlin, Heidelberg: Springer Berlin Heidelberg; 2015:234–241.
- Çiçek Ö, Abdulkadir A, Lienkamp SS, Brox T, Ronneberger O. 3D U-Net: learning dense volumetric segmentation from sparse annotation. In: *Medical Image Computing and Computer-Assisted Intervention – MICCAI*. 2016: 19th International Conference, Athens, Greece, October 17–21, 2016, Proceedings, Berlin, Heidelberg: Springer Berlin Heidelberg; 2016:424–432.
- Roth HR, Oda H, Hayashi Y, et al. Hierarchical 3D fully convolutional networks for multi-organ segmentation. In: *CoRR*. Vol. abs/1704.06382; 2017:arXiv preprint arXiv:1704.06382.
- Jia Y, Shelhamer E, Donahue J, et al. Caffe: convolutional architecture for fast feature embedding. In: *Proceedings of the 22Nd ACM International Conference on Multimedia*. MM '14. New York, NY, USA: ACM; 2014:675–678.
- Otsu N. A threshold selection method from gray-level histograms. *IEEE Trans Syst Man Cybern*. 1979;9:62–66.
- Felzenszwalb PF, Huttenlocher DP. Distance transforms of sampled functions. *Theor Comput*. 2012;8:415–428.
- Dorn S, Chen S, Sawall S, et al. Organ-specific context-sensitive CT image reconstruction and display. In: *Proc. SPIE 10573, Medical Imaging 2018: Physics of Medical Imaging*; 2018.
- Lebedev S, Sawall S, Knaup M, Kachelrieß M. Optimization of the alpha image reconstruction – an iterative CT-image reconstruction with well-defined image quality metrics. *Z Med Phys*. 2017;27:180–192.
- Stierstorfer K, Rauscher A, Boese J, Bruder H, Schaller S, Flohr T. Weighted FBP – a simple approximate 3D FBP algorithm for multislice spiral CT with good dose usage for arbitrary pitch. *Phys Med Biol*. 2004;49:2209–2218.
- Remy-Jardin M, Remy J, Gosselin B, Copin MC, Wurtz A, Duhamel AA. Sliding thin slab, minimum intensity projection technique in the diagnosis of emphysema: histopathologic-CT correlation. *Radiology*. 1996;200:665–671.
- Kawel N, Seifert B, Luetolf M, Boehm T. Effect of slab thickness on the CT detection of pulmonary nodules: Use of sliding thin-slab maximum intensity projection and volume rendering. *Am J Radiol*. 2009;192:1324–1329.
- McCollough C, Leng S, Yu L, Fletcher JG. Dual- and multi-energy CT: principles, technical approaches, and clinical applications. *Radiology*. 2015;276:637–653.
- Krauss B, Schmidt B, Flohr TG. Dual source CT. In: Johnson TR, Fink C, Schönberg S, Reiser MF, eds. *Dual Energy CT in Clinical Practice*. Berlin Heidelberg: Springer-Verlag; 2011:11–20.
- Holmes II DR, Fletcher JG, Apel A, et al. Evaluation of non-linear blending in dual-energy computed tomography. *Eur J Radiol*. 2008;68:409–413.
- Thieme SF, Johnson TRC, Lee J, et al. Dual-energy CT for the assessment of contrast material distribution in the pulmonary parenchyma. *Am J Roentgenol*. 2009;193:144–149.
- Pache G, Krauss B, Strohm P, et al. Dual-energy CT virtual noncalcium technique: detecting posttraumatic bone marrow lesions feasibility study. *Radiology*. 2010;256:617–624.
- Boll DT, Patil NA, Paulson EK, et al. Renal stone assessment with dual-energy multidetector CT and advanced postprocessing techniques: improved characterization of renal stone composition pilot study. *Radiology*. 2009;250:813–820.
- Graser A, Johnson TRC, Bader M, et al. Dual energy CT characterization of urinary calculi: Initial in vitro and clinical experience. *Invest Radiol*. 2008;43:112–119.
- Hidas G, Eliahou R, Duvdevani M, et al. Determination of renal stone composition with dual-energy CT: in vivo analysis and comparison with x-ray diffraction. *Radiology*. 2010;257:394–401.
- Stolzmann P, Leschka S, Scheffel H, et al. Characterization of urinary stones with dual-energy CT: improved differentiation using a tin filter. *Invest Radiol*. 2010;45:1–6.
- Choi HK, Al-Arfaj AM, Eftekhari A, et al. Dual energy computed tomography in tophaceous gout. *Ann Rheum Dis*. 2009;68:1609–1612.
- Manger B, Lell M, Wacker J, Schett G, Rech J. Detection of periarticular urate deposits with dual energy CT in patients with acute gouty arthritis. *Ann Rheum Dis*. 2012;71:470–472.
- Nicolaou S, Yong-Hing CJ, Galea-Soler S, Hou DJ, Louis L, Munk P. Dual energy CT as a potential new diagnostic tool in the management of gout in the acute setting. *Am J Roentgenol*. 2010;194:1072–1078.
- Krauss B, Grant KL, Schmidt BT, Flohr TG. The importance of spectral separation: an assessment of dual-energy spectral separation for quantitative ability and dose efficiency. *Invest Radiol*. 2015;50:114–118.
- Johnson TRC, Krauß B, Sedlmair M, et al. Material differentiation by dual energy CT: initial experience. *Eur Radiol*. 2007;17:1510–1517.
- Chen S, Endres J, Dorn S, et al. *A Feasibility Study of Automatic Multi-Organ Segmentation Using Probabilistic Atlas*. Berlin, Heidelberg: Springer Berlin Heidelberg; 2017:218–223.
- Lavdas I, Glocker B, Kamnitsas K, et al. Fully automatic, multi-organ segmentation in normal whole body magnetic resonance imaging (MRI), using classification forests (CFs), convolutional neural networks (CNNs) and a multi-atlas (MA) approach. *Med Phys*. 2017;44:5210–5220.
- Okada T, Yokota K, Hori M, Nakamoto M, Nakamura H, Sato Y. Construction of hierarchical multi-organ statistical atlases and their application to multi-organ segmentation from CT images. In: Metaxas D, Axel L, Fichtinger G, Székely G, eds. *Medical Image Computing and Computer-Assisted Intervention – MICCAI 2008: 11th International Conference, New York, NY, USA, September 6–10, 2008, Proceedings, Part I*. Berlin, Heidelberg: Springer Berlin Heidelberg; 2008:502–509.
- Park H, Bland PH, Meyer CR. Construction of an abdominal probabilistic atlas and its application in segmentation. *IEEE Trans Med Imaging*. 2004;22:483–492.
- Wolz R, Chu C, Misawa K, Fujiwara M, Mori K, Rueckert D. Automated abdominal multi-organ segmentation with subject-specific atlas generation. *IEEE Trans Med Imaging*. 2013;32:1723–1730.